AGU PUBLICATIONS

JGR

Journal of Geophysical Research: Solid Earth

RESEARCH ARTICLE
10.1002/2014JB011187

Key Points:
- Supershear rupture transitions studied numerically
- For weaker faults, rupture speeds increase continuously to supershear
- For stronger faults, the rupture jumps ahead with negligible slip and slip rate

Supporting Information:
- Readme
- Animation S1
- Animation S2
- Figure S1
- Figure S2

Correspondence to:
C. Liu,
Chao.Liu@earth.ox.ac.uk

Citation:
Liu, C., A. Bizzarri, and S. Das (2014), Progression of spontaneous in-plane shear faults from sub-Rayleigh to compressional wave rupture speeds, *J. Geophys. Res. Solid Earth*, *119*, doi:10.1002/2014JB011187.

Received 11 APR 2014
Accepted 19 OCT 2014
Accepted article online 27 OCT 2014

Progression of spontaneous in-plane shear faults from sub-Rayleigh to compressional wave rupture speeds

Chao Liu[1], Andrea Bizzarri[2], and Shamita Das[1]

[1]Department of Earth Sciences, University of Oxford, Oxford, UK, [2]Istituto Nazionale di Geofisica e Vulcanologia, Bologna, Italy

Abstract We investigate numerically the passage of spontaneous, dynamic in-plane shear ruptures from initiation to their final rupture speed, using very fine grids. By carrying out more than 120 simulations, we identify two different mechanisms controlling supershear transition. For relatively weaker faults, the rupture speed always passes smoothly and continuously through the range of speeds between the Rayleigh and shear wave speeds (the formerly considered forbidden zone of rupture speeds). This, however, occurs in a very short time, before the ruptures reach the compressional wave speed. The very short time spent in this range of speeds may explain why a jump over these speeds was seen in some earlier numerical and experimental studies and confirms that this speed range is an unstable range, as predicted analytically for steady state, singular cracks. On the other hand, for relatively stronger faults, we find that a daughter rupture is initiated by the main (mother) rupture, ahead of it. The mother rupture continues to propagate at sub-Rayleigh speed and eventually merges with the daughter rupture, whose speed jumps over the Rayleigh to shear wave speed range. We find that this daughter rupture is essentially a "pseudorupture," in that the two sides of the fault are already separated, but the rupture has negligible slip and slip velocity. After the mother rupture merges with it, the slip, the slip velocity, and the rupture speed become dominated by those of the mother rupture. The results are independent of grid sizes and of methods used to nucleate the initial rupture.

1. Introduction

It is now known that in-plane shear faults (primarily strike-slip earthquakes) can not only exceed the shear wave speed of the medium but can even reach the compressional wave speed (this is commonly referred to as supershear earthquakes in the geophysical literature or analogously as intersonic ruptures in the framework of fracture mechanics). This result is based on theoretical and numerical studies [*Burridge*, 1973; *Andrews*, 1976; *Das and Aki*, 1977; *Burridge et al.*, 1979; *Freund*, 1979; *Geubelle and Kubair*, 2001; *Bizzarri et al.*, 2001; *Festa and Vilotte*, 2006; *Dunham*, 2007; *Liu and Lapusta*, 2008; *Lu et al.*, 2009], laboratory experiments [*Rosakis et al.*, 1999; *Rosakis*, 2002; *Xia et al.*, 2004, 2005; *Lu et al.*, 2007; *Rosakis et al.*, 2007; *Passelègue et al.*, 2013] and indirect evidence based upon seismic data analysis [*Archuleta*, 1984; *Olsen et al.*, 1997; *Bouchon et al.*, 2001; *Bouchon and Vallée*, 2003; *Dunham and Archuleta*, 2004; *Ellsworth et al.*, 2004; *Robinson et al.*, 2006; *Bhat et al.*, 2007; *Vallée et al.*, 2008].

On the other hand, analytical calculations made on steady state singular cracks [*Broberg*, 1994, 1995, 1999] and numerical studies on spontaneous nonsingular cracks [*Andrews*, 1976] show that speeds between the Rayleigh and shear wave speeds are not possible. In such a case there is negative energy flux into the fault edge from the surrounding medium. The fault would not absorb strain energy but generate it (see *Broberg* [1999] for details). In a pioneering numerical study, *Andrews* [1976] showed that the forbidden zone does exist, even for nonsingular, 2-D, in-plane faults which start from rest and spontaneously accelerate to some terminal velocity. The existence of this "forbidden zone" in rupture speed has been supported by many studies, both analytical [*Burridge et al.*, 1979] and numerical [*Liu and Lapusta*, 2008; *Lu et al.*, 2009]. *Geubelle and Kubair* [2001] studied this problem numerically using a spectral boundary integral equation method. Though they find similar results as above, they do not find the forbidden zone. Instead, they schematically demonstrate that for most of their cases, the rupture front passes rapidly and smoothly through the forbidden zone, although the initiation procedure of the rupture is not described in detail, and the (numerical) resolution of the forbidden zone is not shown. They also do not clarify why this happens for some configurations and their insights are retrieved from the location (and shape) of the rupture front (and not from a formal computation of the rupture speed).

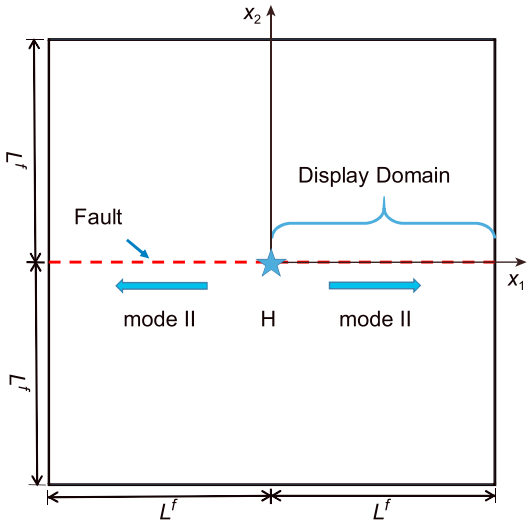

Figure 1. Geometry of the fault. The dotted line indicates the fault trace. The rupture begins at the hypocenter *H* and propagates bilaterally, as shown by the arrows. L^f is the half length of the fault. Due to the symmetry of the problem, only one half of the fault is considered (as indicated).

Recently, *Bizzarri and Das* [2012] showed that the rupture front actually does pass through the $[v_R, v_S]$ range of speeds, and very fast. Unprecedented fine grids are used in their numerical experiments for a truly 3-D shear ruptures (in which the in-plane (mode II) and the antiplane (mode III) are mixed together) propagating on a planar fault and obeying the linear slip-weakening governing model.

Motivated by these results, here we examine in detail, using very fine grids, the 2-D pure mode II case to see the passage of the rupture front from sub-Rayleigh to the compressional wave speeds. The 2-D problem is of interest because for very long strike-slip faults in the Earth's crust the rupture becomes primarily pure mode II at large distances from the hypocenter (that is, when the fault length is much larger than its width). In addition to the inherent theoretical issues, the interest in supershear ruptures is motivated by very practical implications. Compared to subsonic events, the supershear ruptures produce stronger shaking farther from the fault and are richer in high frequencies [*Aagaard and Heaton*, 2004; *Bhat et al*., 2007; *Bizzarri and Spudich*, 2008; *Bizzarri et al*., 2010].

To investigate the entire range of possible rupture speeds from rupture initiation to the compressional wave speed, numerical experiments are carried out to mainly cover the parameter space where supershear rupture propagation could occur. A few cases where the rupture speed remains below the Rayleigh wave speed are also studied. The small grid sizes used in this study provide a very good resolution of the rupture speed, allowing us to examine the details of the rupture progress from sub-Rayleigh to compressional wave speeds. It is worthwhile to emphasize here that most of the previous studies, instead of showing the actual values of the rupture speeds obtained through numerical calculations, merely plot schematic figures of the rupture speed evolution. *Liu and Lapusta* [2008] and *Lu et al*. [2009] show the rupture speeds, averaged over a broad moving window.

The present paper is organized as follows. In section 2 we present the geometry of the problem. The numerical results are shown in section 3, where we present the two different mechanisms which control the supershear transition. In section 4 we discuss the distance from the nucleation patch at which the supershear transition occurs, and we present a phase diagram to compare against previous results of *Andrews* [1976] and summarize the major conclusions of this study. Technical details on the estimate of the rupture speed, the effect of nucleation methods, and different spatial grid sizes are thoroughly discussed in the three appendices (Appendix A–Appendix C, respectively).

2. Fault Geometry and Rupture Nucleation

In the present study we consider a 2-D, pure in-plane shear (mode II) rupture problem, as shown in Figure 1. The rupture propagates along x_1; the solutions (e.g., the displacement discontinuity) do not depend on x_2 and have only one component (e.g., $u_1(x_1, t)$; for the sake of simplicity, in the remainder of the paper we will omit the subscripts). The elastodynamic problem, in which body forces are neglected, is numerically solved by using the finite difference code described in *Bizzarri et al*. [2001], originally developed by *Andrews* [1973], which uses a mesh of triangles and the leap-frog scheme. The code has been made more efficient by us using parallelization through the OpenMP paradigm. We assume that the fault obeys the linear slip-weakening friction law [*Ida*, 1972], which is expressed by the following relation: $\tau(u) = \sigma_n^{\text{eff}}[\mu_u - (\mu_u - \mu_f)min(u, d_0)/d_0]$, where τ is the magnitude of the shear stress on the fault, σ_n^{eff} is the effective normal stress (assumed to be constant through time), μ_u is the static friction coefficient, μ_f is the dynamic friction coefficient, u is the fault slip, and d_0 is the characteristic slip-weakening distance. The parameters used in this study are listed in Table 1.

Table 1. Parameters Adopted for the 126 Cases in This Study[a]

Parameter	Value
Lamé's constants, $\lambda = G$	35.9 GPa
S wave speed, v_S	3.464 km/s
Rayleigh speed, v_R	3.184 km/s
Eshelby speed, $v_E = \sqrt{2}v_s$	4.899 km/s
P wave speed, v_P	6 km/s
Effective normal stress, σ_n^{eff}	120 MPa
Initial shear stress (prestress), τ_0	73.8 MPa
Dynamic friction coefficient, μ_f	0.46
Dynamic friction level, τ_f	55.2 MPa
Dynamic stress drop, $\tau_0 - \tau_f$	18.6 MPa
Characteristic slip-weakening distance, d_0	0.4 m
$C = v_P\Delta t/\Delta x$[b]	0.0514

[a]We consider homogeneous properties and a constant effective normal stress. Except for C, all parameters are the same as in *Bizzarri and Das* [2012].
[b]Δt is the time step and Δx is the spatial grid length.

Choices of the ratio $C = v_P\Delta t/\Delta x$ and possible rupture speed values that can be resolved numerically are discussed in detail in the Appendix A (Δt and Δx are the temporal and the spatial grid sizes, respectively). For the second-order accurate, explicit, 2-D finite difference scheme employed here, the Courant-Friedrichs-Lewy condition is $C \leq 0.71$ [*Mitchell*, 1976] and ensures the stability and the convergence of the numerical solution. We can choose C or Δt as small as we like, as long as rounding and magnification errors remain negligible.

In order to initiate a rupture governed by the linear slip-weakening friction law, we use an (artificial) nucleation procedure to trigger the dynamic propagation. Once the nucleation stage is completed, the rupture propagates spontaneously. The rupture speed v_r is not prescribed (as for nonspontaneous problems) but is a part of the solution itself. In the present paper we adopt two rupture nucleation strategies with different initial parameters. In the first strategy, called the time-weakening initiation, the rupture is initially nonspontaneous and it propagates at a constant, prescribed rupture speed $v_r = v_{\text{init}}$ [*Andrews*, 1985; *Bizzarri*, 2010]. Values of v_{init} equal to 1.2 km/s and 5 km/s are tested. In the second strategy, called the asperity initiation, a small perturbation in initial shear stress is used to trigger the dynamic rupture [*Bizzarri*, 2010]. The size of the asperity should be small enough to avoid interference with the subsequent spontaneous rupture propagation. The details of the methods and their effect, if any, are fully discussed and quantitatively compared in Appendix B.

3. Numerical Results for 2-D Spontaneous Rupture Propagation

One hundred and twenty six numerical experiments are carried out in this study. They are sorted into six Configurations, named as A to F. For each configuration we investigate the relation existing between the rupture speed and the strength parameter S, originally defined by *Hamano* [1974] as $S = (\tau_u - \tau_0)/(\tau_0 - \tau_f)$, where $\tau_u = \mu_u\sigma_n^{\text{eff}}$ is the upper yield stress, τ_0 is the initial shear stress, and $\tau_f = \mu_f\sigma_n^{\text{eff}}$ is the residual shear stress. The numerator represents the so-called strength excess (i.e., the amount of stress needed to reach the failure point) and the denominator represents the dynamic stress drop. Thus, doubling the value of this stress drop simply reduces S by a factor of 2. In addition, a fault with the same strength would have a different value of S if its initial stress is changed. From here on, we shall refer to weaker/more stressed or a relatively weaker fault as a "weak fault" and vice versa for a "strong fault."

We consider 24 values of S in the range between 0.38 and 1.2, and 6 values larger than 1.2. To obtain different values of S, we change the upper yield stress τ_u, and we keep the other parameters unchanged. Contrary to the 3-D case, where the absolute values of the stresses affect the behavior of the propagating rupture (they indeed

Table 2. Parameters Used in Configurations A to E[a]

Configuration	Δx (m)	Δt (s)	Number Of Cases	Nucleation Method
A	40	3.42×10^{-4}	24	TW[b]: v_{init} = 0.5 km/s
B	20	1.71×10^{-4}	24	〃
C	10	8.57×10^{-5}	24	〃
D	40	3.42×10^{-4}	24	TW[b]: v_{init} = 1.2 km/s
E	40	3.42×10^{-4}	24	Asperity

[a]The fault half-length L^f = 40 km is used for all the configurations.
[b]TW: Time-weakening with starting speed v_{init}.

Table 3. Parameters Used in Configuration F[a]

Strength Parameter S	Δx (m)	Δt (s)	Time (s)	Fault Half Length (km) L^f	Supershear Rupture
1.3	40	3.42×10^{-4}	16	66	Yes
1.4	40	3.42×10^{-4}	16	52	No
1.5	40	3.42×10^{-4}	16	52	No
1.6	160	1.37×10^{-3}	68	214	No
1.7	160	1.37×10^{-3}	68	214	No
1.8	160	1.37×10^{-3}	68	214	No

[a]The time-weakening initiation method with v_{init} = 0.5 km/s is used for all the cases.

control the level of rake rotation; *Bizzarri and Cocco* [2005]), in the 2-D case only the value of S controls the rupture behavior. For $S \geq \sim 1.77$ the rupture speed remains below the Rayleigh wave speed [*Andrews*, 1976; *Das*, 1976; *Das and Aki*, 1977], so most of the values chosen ensure that supershear rupture speeds are attained. Configurations A–C use the same time-weakening initiation strategy with starting speed v_{init} = 0.5 km/s, but

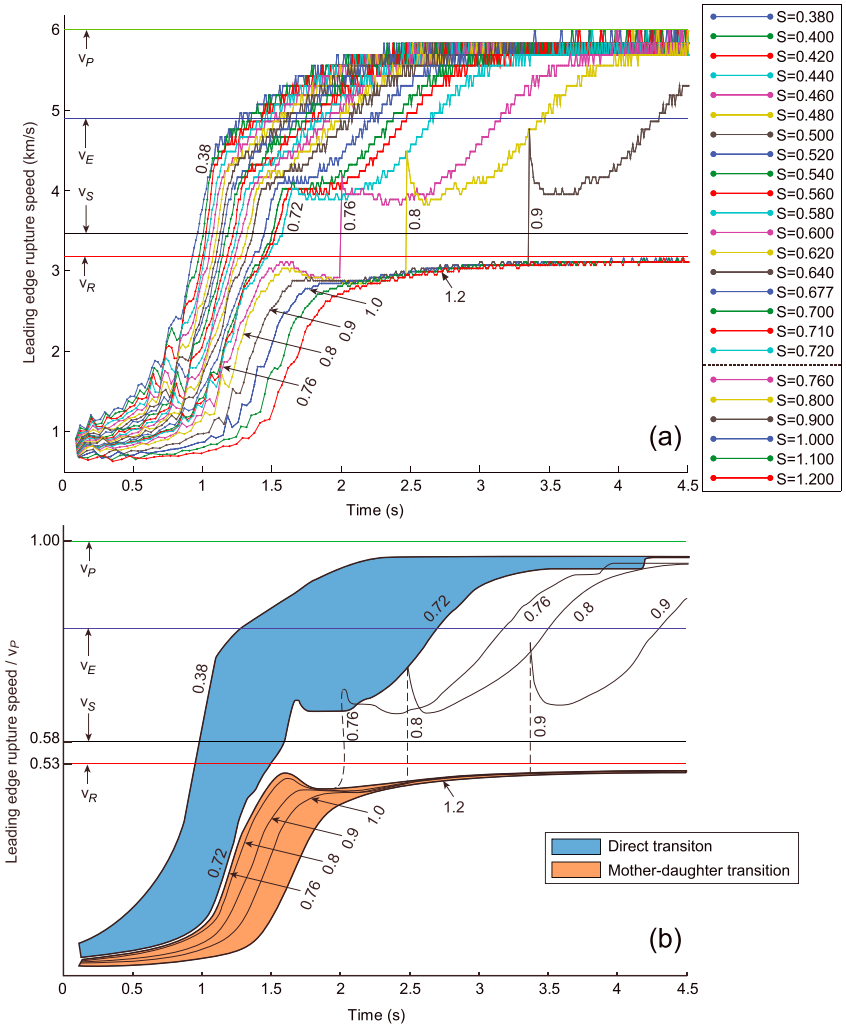

Figure 2. (a) Rupture speeds for the 24 values of S used in Configuration A. The spatial grid size Δx is 40 m, and the starting velocity is 0.5 km/s. The range $[v_R, v_S]$ is marked. The two kinds of transition behavior for the smaller and larger S values are clearly seen (light blue and light orange, respectively). (b) Schematic version of Figure 2a, which emphasizes the two rather distinct behaviors. The vertical dashed lines indicate the birth of the daughter rupture. For values of S greater than 0.9 the jump to the supershear speed (associated with the presence of the forbidden zone) occurs after t = 4.5 s. When S reaches the critical value of 1.77 [*Andrews*, 1976], the rupture asymptotically reaches v_R and remains in the sub-Rayleigh regime.

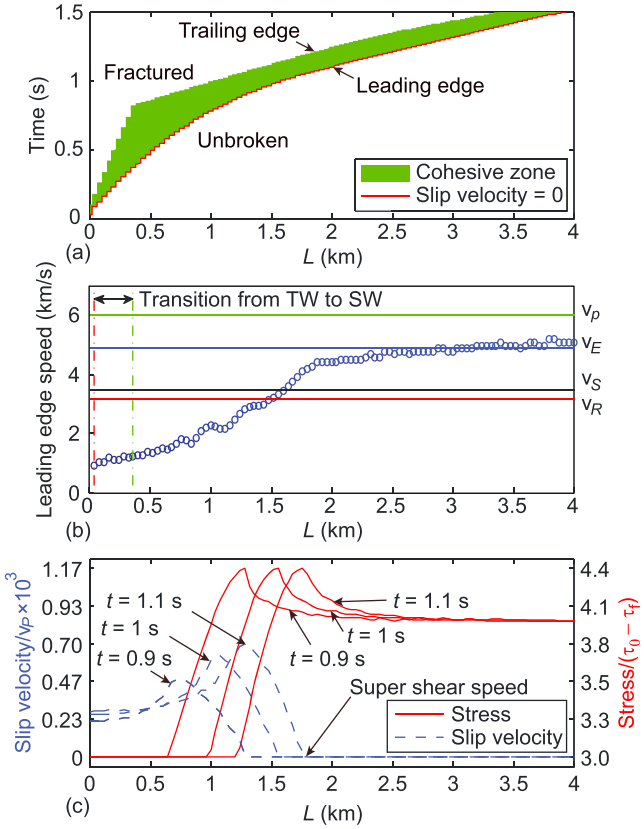

Figure 3. Cohesive zone and rupture speed for the case $S = 0.4$ of Configuration A. (a) The green region indicates the cohesive zone, and the red line indicates where slip velocity is zero (i.e., the boundary between the unbroken and the broken parts of the fault). Leading edge and trailing edge of the cohesive zone are also indicated, in agreement with *Bizzarri and Das* [2012]. (b) Rupture speed as a function of the distance from the hypocenter. The red and green vertical dashed lines denote the beginning of slip weakening (SW) and the end of time weakening (TW). Region between red vertical line and green vertical line denotes the transition from TW to SW. For distances greater than the green vertical line the propagation is fully spontaneous. (c) Stress (normalized by the dynamic stress drop) and fault slip velocity (normalized by v_P) at different times $t = 0.9$ s, 1 s, and 1.1 s, which correspond to times before, during, and after the transition, respectively. The position of the rupture tip with supershear rupture speed is indicated.

different spatial grid sizes, $\Delta x = 40$ m, 20 m, and 10 m. Configurations D and E use the same spatial grid length $\Delta x = 40$ m as Configuration A, but different nucleation methods. Configuration D uses the time-weakening initiation strategy with starting speed $v_{\text{init}} = 1.2$ km/s, and Configuration E uses the asperity initiation strategy. The relevant parameters for these six Configurations are listed in Table 2. For comparison, we also study six cases ($S > 1.2$) where it is difficult or impossible for the rupture speed to exceed the Rayleigh wave speed. These cases are grouped together in Configuration F. For the cases with $S > 1.6$, we used larger spatial grids ($\Delta x = 160$ m) as it takes longer for the rupture to propagate (the parameters are given in Table 3).

3.1. Supershear Rupture for Weaker Faults (~0.38 ≤ S ≤ ~0.72): The Direct Transition Mechanism

For this range of S the fault is relatively weak and the supershear rupture occurs soon after nucleation. We choose $S \geq 0.38$ as lower boundary of this interval simply to give enough time for the rupture to become spontaneous and to avoid any possible artificial effect of the nucleation methods. The rupture speed versus time for this range of S is shown in Figure 2a, with a schematic summary version shown in Figure 2b. This figure pertains to $\Delta x = 40$ m, but the results for $\Delta x = 20$ m and $\Delta x = 10$ m are very similar (see the results shown in Appendix C), which indicates that our conclusions are independent of the spatiotemporal grid lengths.

The rupture speed curves for this range of S in Figure 2a form a completely separate group (light blue in Figure 2b) from faults with larger values of S (light orange in Figure 2b). We see that the rupture starts from rest, accelerates and passes smoothly through the range $[v_R, v_S]$, and then approaches the compressional wave speed v_P. This direct transition mode has been studied by [*Geubelle and Kubair*, 2001; *Festa and Vilotte*, 2006; *Dunham*, 2007; *Liu and Lapusta*, 2008; *Lu et al.*, 2009]. The prominent result to be highlighted here is that the forbidden zone has been shown to or implied to exist for this range of S in some of these studies [*Liu and Lapusta*, 2008; *Lu et al.*, 2009]. The present study—which adopts very fine grids with a proper rupture speed resolution in the $[v_R, v_S]$ (see Appendix A)—quantitatively demonstrates that the rupture speed evolves continuously and passes through this range of rupture velocities during direct transition. For such faults the rupture speed continuously increases from sub-Rayleigh to supershear without any jump. We also see (Figure S1 in the supporting information) that the time spent in the $[v_R, v_S]$ regime is independent of the grid size.

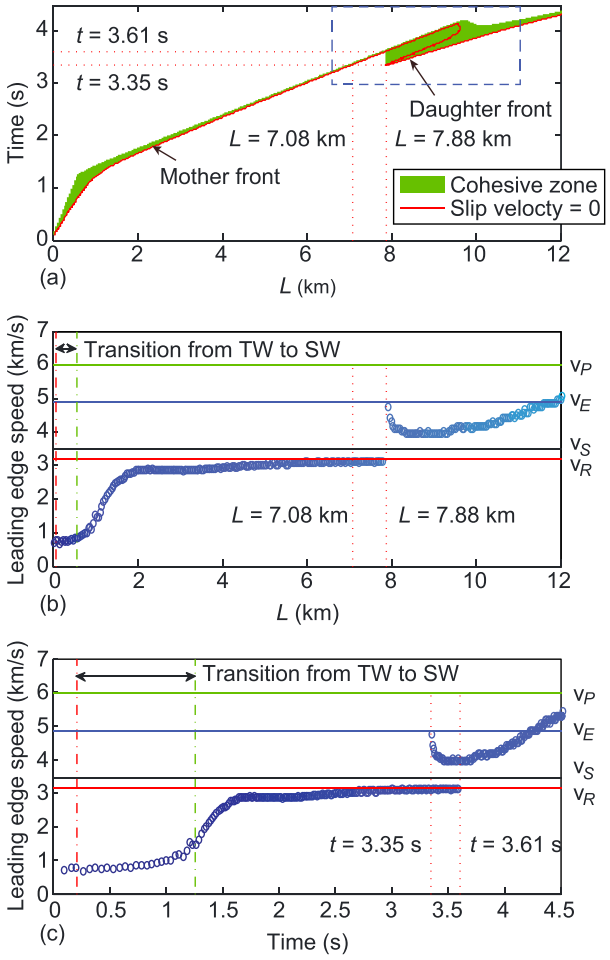

Figure 4. (a and b) The same as for Figure 3 but now for $S = 0.9$. (c) Speed versus time. Details of the daughter rupture, marked by a rectangle in Figure 4a, are shown in Figure 5.

As an example, details of the case $S = 0.4$ are shown in Figure 3. In Figure 3a, we plot the evolution of the cohesive zone, where the fault traction degrades from the upper yield stress down to the kinetic level (or analogously, where the fault slip increases from 0 to d_0). *Bizzarri et al.* [2001] and *Bizzarri and Das* [2012] quantify its length as X_b, the breakdown zone length, and its duration as T_b, the breakdown time. From Figures 2 and 3a it is clear that no daughter rupture develops ahead of the main rupture, which indeed is a single continuous line, without any jump. The position of the leading edge and rupture time increases smoothly during the transition. Remarkably, the rupture speed increases continuously and penetrates into the $[v_R, v_S]$ region roughly at a distance of 1.5 km from the hypocenter (Figures 3a and 3b). Numerical details for the computation of the rupture speed are reported in Appendix A.

In Figure 3c, we plot the stress and fault slip velocity at three different times, $t = 0.9$ s, 1 s, and 1.1 s, which correspond to the time before, during, and after the transition, respectively. It is obvious that no shear stress peak is developed ahead the main rupture tip, contrary to the situation shown in *Andrews* [1976, Figures 4–6], and which pertain to the mother-daughter transition mechanism (see next section). From Figure 3c the rupture tip is easily identifiable from the slip velocity curves. The movie showing the complete time evolution of stress and fault slip velocity is available as Animation S1 in the supporting information.

3.2. Supershear Rupture for Stronger Faults ($S \geq$~0.76): The Mother-Daughter Transition Mechanism

For $S \geq 0.76$ Figure 2 shows that the fault rupture behavior is quite different compared to that discussed in section 3.1. Although the fault is now stronger, the overall behavior of the rupture below v_R is similar to that seen above. However, as v_R is approached, a major change in the behavior occurs: the rupture speed no longer crosses v_R but approaches it asymptotically.

In this range of the parameter space, the mother-daughter transition mechanism (reported earlier by *Andrews* [1976], *Dunham* [2007], and *Lu et al.* [2009]), a secondary fracture is initiated ahead of the main rupture front. Animation S2 in the supporting information is the movie of the time evolution of stress and fault slip velocity. For the cases $S \geq 0.9$, we see the rupture asymptotically approaches v_R and then the jump described above occurs. The daughter rupture now starts to propagate at a speed which is already supershear, but it exhibits negligible fault slip and fault slip velocity (Figures 5b–5d). The mother rupture then merges with the daughter rupture at (Figures 4a and 5a), and it is only after this time that the fault slip and the fault slip velocity of the daughter rupture become appreciable. In fact, the increase in the speed of the daughter rupture mentioned above actually occurs after the merging of the two ruptures and eventually itself approaches the *P* wave speed (the limiting speed of this rupture mode). Thus, the daughter rupture is essentially a "pseudorupture," where the two sides of the fracture have broken apart, but do not have significant motion and no appreciable stress drop, a feature seen in *Andrews* [1976].

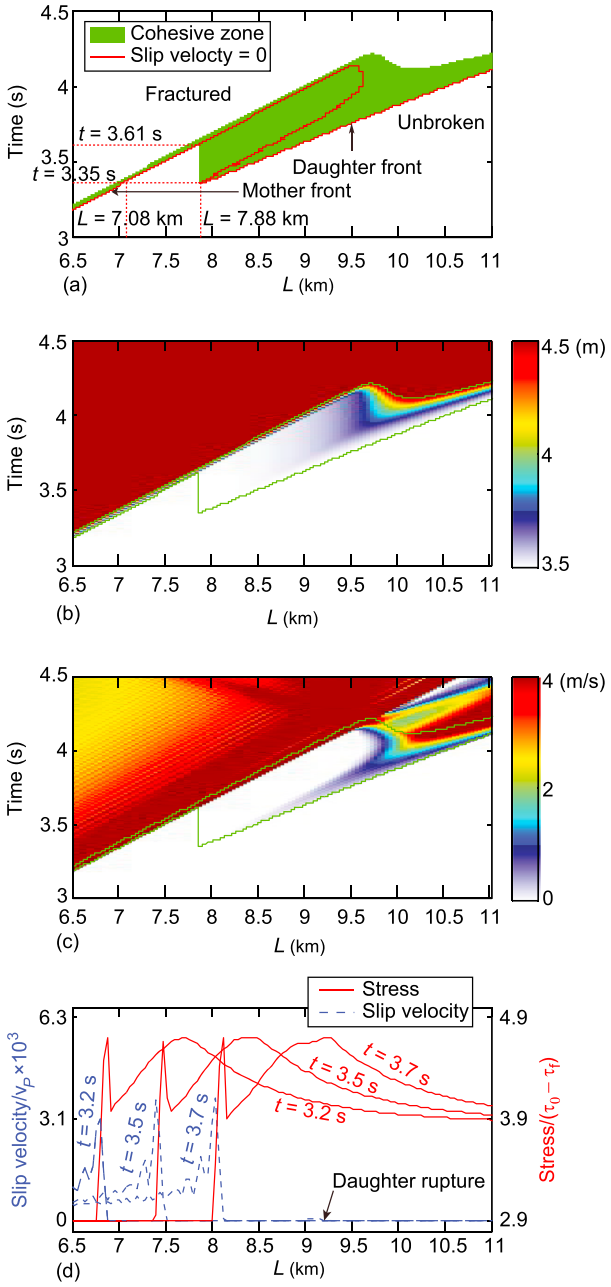

Figure 5. (a) Cohesive zone, (b) fault slip in m, and (c) fault slip velocity in m/s zooming in on the daughter rupture portion of Figure 4 ($S = 0.9$ of Configuration A). In Figures 5b and 5c the thick green line marks the cohesive zone. (d) Snapshots of stress and slip velocity at times $t = 3.2$ s, 3.5 s, and 3.7 s which correspond to times before, during, and after the transition, respectively. The position of the daughter rupture tip is indicated.

For cases with $\sim 0.76 \leq S < 0.9$, the fault rupture behavior is similar to $S = 0.9$, but there is a decrease in rupture speed as it approaches the Rayleigh wave speed, this being more obvious for smaller S values in this range. For $S > 0.9$ we still have a jump from the sub-Rayleigh to the supershear regime.

4. Discussion and Conclusions

In the present paper we consider 2-D, pure in-plane shear (mode II) ruptures, spontaneously propagating and obeying the linear slip-weakening governing model [*Ida*, 1972]. We thoroughly analyze the behavior of the rupture front and the cohesive zone where the stress is released, in order to see whether (i) the rupture jump and (ii) the so-called forbidden zone (between the Rayleigh and the shear wave speeds, v_R and v_S, respectively), previously reported (*Andrews* [1976] among many others referenced above) for this kind of problem, really exist.

We scrutinize the different behavior of the ruptures by considering a large number of values of the parameter S ranging from 0.38 to 1.8. We conduct all the numerical experiments by employing a very fine spatiotemporal resolution, to capture all the details of the traction evolution within the cohesive zone and to guarantee an excellent resolution of the $[v_R, v_S]$ velocity range. On average, we have about 25 spatial grids inside the cohesive zone before supershear transition occurs.

The simulations confirm that there are two rather different mechanisms which control the supershear transition. For weaker faults ($S < \sim 0.7$), the direct transition mechanism [*Liu and Lapusta*, 2008; *Lu et al.*, 2009] dominates (light blue in Figure 2a). There is no peak in the shear stress field traveling ahead of the main rupture front, and therefore, no daughter rupture appears (see Figure 3 and Animation S1 in the supporting information). This mechanism is in agreement with the numerical results obtained at very low effective normal stress by *Lu et al.* [2009, section 3.2]. More importantly, we have shown here that in this case, referred to as direct transition, the rupture penetrates and then passes smoothly through the formerly considered forbidden zone. It then approaches the compressional wave speed (the terminal, limiting speed for this rupture mode). In other words, we quantitatively demonstrated for the first time here that, even in 2-D, the penetration of the $[v_R, v_S]$ range occurs, as for truly 3-D ruptures [*Bizzarri and Das*, 2012]. Remarkably,

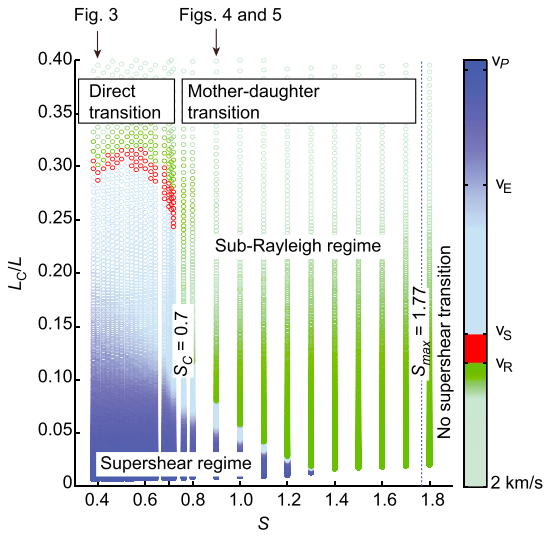

Figure 6. Phase diagram summarizing the behavior of all the cases in Configurations A and F. We plot the strength parameter S on the abscissa, the ratio between the critical length L_c and the location of the rupture front L on the ordinate. The relevant cases reported in Figures 3–5 are also indicated.

the forbidden zone can disappear, and it is not a universal feature of mode II, nonsingular ruptures. The results are accurate and robust; the phenomenon we observe is not an artifact of the numerical method, the numerical resolution, or the method employed to nucleate the rupture.

For stronger faults ($S > \sim 0.7$), the mother-daughter mechanism (also referred to as the Burridge-Andrews mechanism) [*Andrews*, 1976; *Freund*, 1979; *Abraham and Gao*, 2000; *Rosakis*, 2002; *Dunham*, 2007] dominates in this mechanism. The forbidden zone does exist as the transition to the intersonic regime involves a rupture speed jump.

In Figure 6 we report a phase diagram summarizing the behavior of the different ruptures considered in the present work. As S increases and approaches the critical value $S_{max} = 1.77$ the rupture tends to remain in the sub-Rayleigh regime. On the other hand, when S decreases, the supershear transition can occur sooner. The passing of the rupture through the $[v_R, v_S]$ velocity range occurs for the values of S smaller than the critical value $S_c = \sim 0.7$, identified above as the boundary between the direct transition ($S < S_c$) and the mother-daughter transition mechanism ($S > S_c$). Figure 6 also shows the distance at which the supershear transition occurs, namely, the transitional length $L_{trans}^{(2-D)}$ of *Bizzarri and Das* [2012], and that $L_{trans}^{(2-D)}$ does not linearly depend on S over the whole parameter space.

In the present paper we employ the linear slip-weakening law, which is known to be a very simplified, idealized version of more elaborate (realistic) governing equations (see *Bizzarri* [2011] for a review). It is possible to simulate spontaneous supershear rupture propagation with other constitutive models (see Table 1 of *Bizzarri* [2011, and references cited therein]). Therefore, one intriguing question which naturally emerges is whether the disappearance of the forbidden zone of rupture speeds we observe in this study in the case of the linear slip-weakening law is a common feature of all constitutive models. This could be the subject of future investigations.

It is very important to note that the results presented and discussed here are not in conflict with previous theoretical predictions for 2-D problems [e.g., *Burridge et al*., 1979; *Freund*, 1979; *Broberg*, 1994, 1995, 1999]. The latter establish the existence of the forbidden zone of rupture speeds for singular, steady state cracks, while our simulations refer to nonsingular, nonsteady, spontaneous ruptures. However, there is no question that the $[v_R, v_S]$ range of rupture speeds is one within which the rupture does not linger (also seen for the 3-D case by *Bizzarri and Das* [2012]), showing that it is truly an unstable zone. In fact, the only possible terminal speeds of ruptures are either the Rayleigh wave speed for relatively stronger faults or the compressional wave speed for the relatively weaker faults, and no other. We also note that in the range $[v_S, v_P]$, the rupture speed continuously increases (Figure 2b), though slowly, and only starts leveling off once it nears the compressional wave speed. Thus, earthquake ruptures would probably not travel large distances in the $[v_S, v_P]$ velocity range.

Finally, our study uses a constant value of S over the entire fault, whereas in the real Earth S could vary along a fault. So, a fault would slow down and speed up many times during the faulting process. This could explain why supershear ruptures are rarely observed. In addition, the fault in our model remains planar, whereas real faults could change strike and deviate very frequently from planarity, exhibiting geometrical complexities such as bending, branching, and kinks [*Aochi et al*., 2000; *Poliakov et al*., 2002; *Kame et al*., 2003; *Fliss et al*., 2005; *Robinson et al*., 2006, 2010; *Bhat et al*., 2007]. This additional complexity might also affect the supershear transition mechanism [e.g., *Bouchon et al*., 2001; *Robinson et al*., 2006].

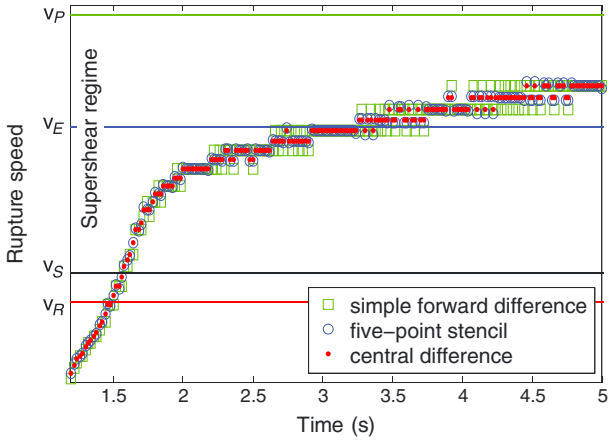

Figure A1. Rupture speed, estimated using the two-point forward difference method (green squares), two-point central difference method (red dots), and five-point stencil difference (blue circles) are shown (see Appendix A for details). Similar results are obtained using $\Delta x = 20$ m and $\Delta x = 10$ m.

Appendix A: Estimate of the Rupture Speed in 2-D Numerical Experiments and Its Limitations

A1. Estimation of the Rupture Speed in 2-D

Rupture speed is an indirect part of the solution of the spontaneous rupture propagation problem which has to be retrieved from the rupture times. Such a computation, although conceptually straightforward it is not numerically simple. In this section we test different methods in order to explore whether the results depend on the assumed numerical algorithm.

By adopting the two-point forward difference method, the rupture speed $v_r(i)$ at a generic fault node i (having absolute coordinate $x_i = i\Delta x$) is

$$v_r(i) = \frac{(i+1)\Delta x - i\Delta x}{t_r(i+1) - t_r(i)} = \frac{\Delta x}{t_r(i+1) - t_r(i)} \tag{A1}$$

where Δx is the spatial grid length, $t_r(i)$ represents the rupture time at node i. According to previous study [*Bizzarri and Das*, 2012, and references cited therein], the rupture time at node i is defined as the first time at which the fault slip velocity in that location exceeds the threshold value $v_l = 0.01$ m/s. (Readers can refer to section 3.1 of *Bizzarri* [2013] for a discussion.)

Similarly, in the two-point central difference method, the rupture speed $v_r(i)$ at node iΔx is

$$v_r(i) = \frac{(i+1)\Delta x - (i-1)\Delta x}{t_r(i+1) - t_r(i)} = \frac{2\Delta x}{t_r(i+1) - t_r(i-1)} \tag{A2}$$

In the five-point stencil difference method, the rupture speed $v_r(i)$ at node $i\Delta x$ is

$$\begin{aligned} v_r &= \frac{(i-2)\Delta x - 8(i-1)\Delta x + 8(i+1)\Delta x - (i+2)\Delta x}{t_r(i-2) - 8t_r(i-1) + 8t_r(i+1) - t_r(i+2)} \\ &= \frac{12\Delta x}{t_r(i-2) - 8t_r(i-1) + 8t_r(i+1) - t_r(i+2)} \end{aligned} \tag{A3}$$

All of these three direct estimation methods are tested, and the results are shown in Figure A1. Rupture speeds obtained by using the different methods are found to be very similar for the present 2-D configurations, but the two-point central difference method is preferred; it has less numerical oscillations than the simple forward different scheme, and it is practically identical to the five-point stencil, but it is computationally more efficient.

A linear interpolation method was suggested by the associate editor to reduce the discreteness of rupture speed, which is discussed in section A2. Consider the first time step when the slip velocity becomes nonzero. Define a "virtual traction" that varies linearly in time between the value of traction at the previous time step and the value of the "trial traction" [*Andrews*, 1999] at the current time step. Find the (nondiscrete) time when this virtual traction equals the upper yield stress. Owing to the linear interpolation assumption, this time lies between the current and previous time steps. Hence, a subsample-precision rupture time and speed can be obtained by assuming linear interpolation of tractions between time steps.

A2. Possible Values of Rupture Speeds Obtainable in the 2-D Numerical Experiments

Since the rupture speeds v_r determined from discrete grids in the space-time numerical scheme are limited to certain discrete values, it is important scrutinize what these possible values are. In Figure A2 some possible values of v_r are schematically indicated by using the two-point central difference method (which is our

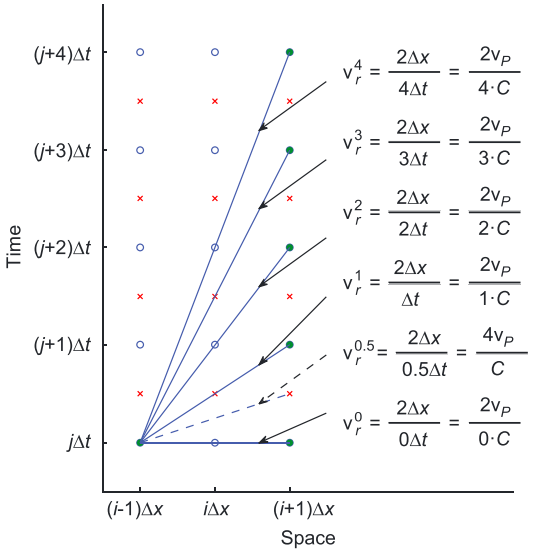

Figure A2. Rupture speed estimation by two-point central difference. Integers *i* and *j* discretize the space and the time domains, respectively.

preferred method; see section A1). The largest v_r is $v_r^0 = \infty$, obtained when the node $(i-1)\Delta x$ and $(i+1)\Delta x$ fail at the same time (horizontal line). The second largest v_r is $v_r = 2v_P/C$, where $C = v_P\Delta t/\Delta x$, when node $(i-1)\Delta x$ and $(i+1)\Delta x$ fail at $i\Delta t$ and $(i+1)\Delta t$, respectively (or fail at $(i-1)\Delta t$ and $i\Delta t$, situation not shown in Figure A2 in the interest of simplicity). If a possible value between v_r^0 and v_r^1 is needed, for example, $v_r^{1/2} = 4v_p/C$, we have to change the time step from Δt to $1/2\Delta t$ to add a node $(j+1/2)\Delta t$ between $i\Delta t$ and $(j+1)\Delta t$. These new nodes for the new time step $1/2\Delta t$ are indicated by crosses in Figure A2. Note that if the spatial grid size is changed from Δx to $1/2\Delta x$ simultaneously, the desired value $v_r^{1/2} = 4v_P/C$ will be unavailable again.

To fully understand the limitation in the numerical resolution of the rupture speeds, we express the quantity $t_r(i+1) - t_r(i-1)$ in equation (A2) as $N \times \Delta t (N = 0, 1, 2, 3, \ldots)$, so that the only possible discrete values of the rupture speeds that can be determined from the discrete grids in the space-time are

$$v_r^N = \frac{\Delta x}{N \times \Delta t} = \frac{v_P}{N \times C}, \quad N = 0, 1, 2, 3, \ldots \tag{A4}$$

where $v_r^N = \left\{v_r^0, v_r^1, v_r^2, \ldots v_r^\infty\right\}$ represent the only possible discrete values of the rupture speed grid. For a given pair of Δx and Δt, and for a given numerical algorithm to compute the rupture speed (see section A1), v_r^N are determined by the value $\Delta t/\Delta x$ or by C. Figure A3 shows the rupture speed grid v_r^N from different C in 2-D numerical experiments. For smaller C, the grid points are denser and more evenly distributed in the interval of interest, which implies a better resolution of the forbidden zone. In the interval $[v_R, v_S]$ the number of possible discrete rupture speed values increases from 1 to 6 as C decreases from 0.9 to 0.0541. We use $C = 0.0514$ in this study as the speed interval of interest is well covered by the grid points and the forbidden zone is well resolved by six grid points.

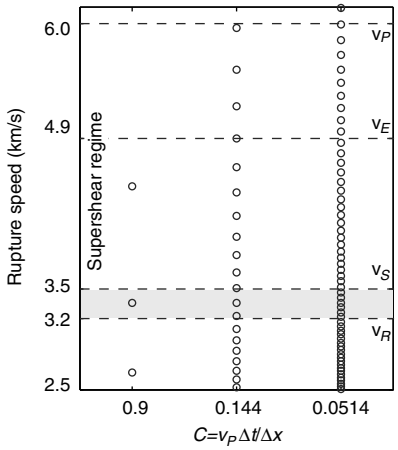

Figure A3. The only possible rupture speed values that can be obtained with the two-point central difference method and using different values of *C*. As *C* increases, the grid points are more evenly distributed. $C = 0.9$ and 0.144 are the values used in *Andrews* [1973, 1976] and *Bizzarri and Das* [2012], respectively. $C = 0.05$ is used in this study. The range of velocities formerly considered forbidden is shown in gray.

Thus, for a given spatial grid length Δx the rupture speed resolution could be improved by using smaller Δt, as long as the Courant-Friedrichs-Lewy condition is satisfied. It is interesting to emphasize here that if we concurrently reduce Δx and Δt by keeping C unchanged, it is not possible to improve the rupture speed resolution. Finally, we remark that the numerical algorithm employed to compute the rupture speed can also affect the possible discrete rupture speed values (see Figure A1), and ultimately the resolution within the forbidden zone. Thus, the direct estimation methods are less important than the values of $\Delta t/\Delta x$ or C.

The rupture speed resolution could also be improved by using the linear interpolation method without changing the $\Delta t/\Delta x$ or C. We do not see more noisy rupture speeds in our test cases but this is not necessarily guaranteed in other simulation methods and codes. We suggest using the interpolation method after it is validated by the direct method.

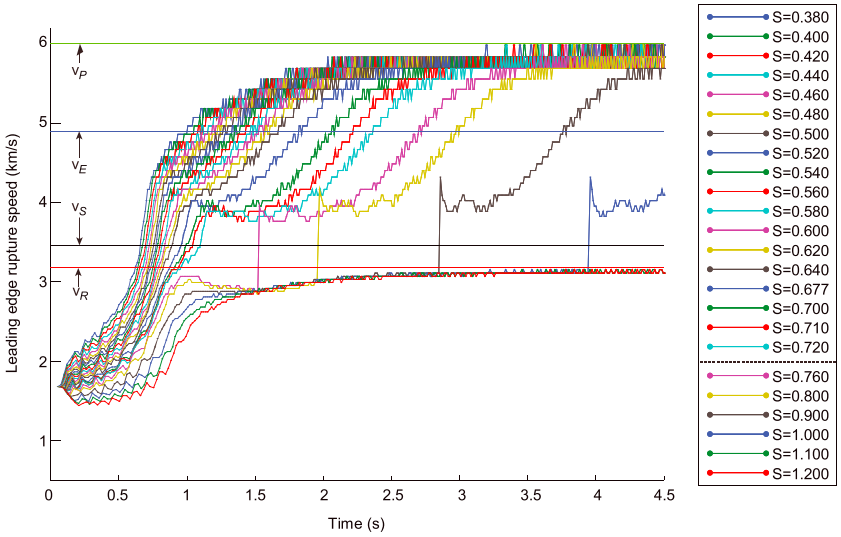

Figure B1. Rupture speeds for different S in Configuration E, in which the rupture nucleation is obtained though the time-weakening method. The Δx is 40 m, and the starting velocity is 1.2 km/s (see Appendix B for further details).

We emphasize that the existence of the forbidden zone shown or implied in a very large number of previous numerical studies dealing with nonsingular 2-D ruptures is possibly related to the lack of resolution of rupture speed in the $[v_R, v_S]$ range.

Appendix B: Effect of Different Nucleation Methods

As well known [see, e.g., *Bizzarri*, 2010], the linear slip-weakening constitutive equation requires the introduction of an artificial procedure to induce the nucleation of the rupture and the subsequent dynamic, spontaneous propagation of the fault surface. Here we scrutinize whether the adopted nucleation strategy can have some influence on the supershear rupture transition and thus on the penetration of the $[v_R, v_S]$ range. To this goal we used two rather different ways for the rupture initiation; the time-weakening method and the asperity method (readers can refer to "Initially non-spontaneous rupture propagation and

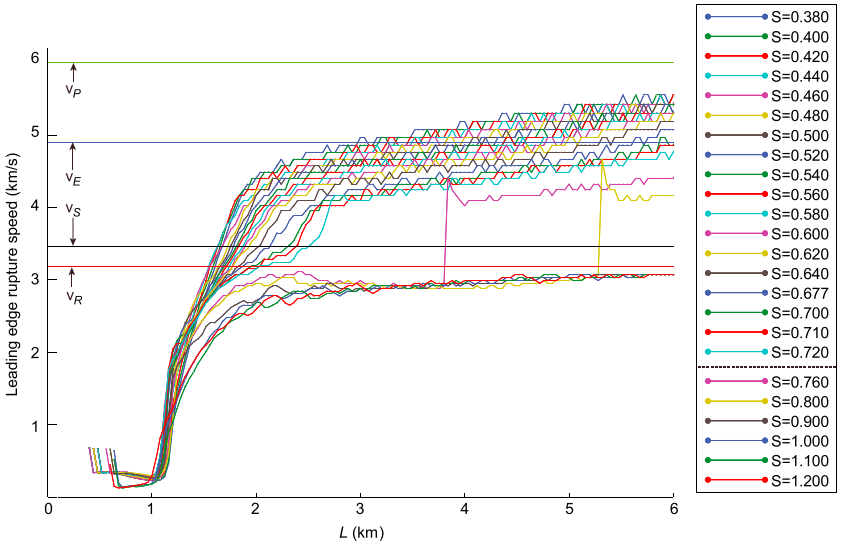

Figure B2. The same as for Figure B1 but now for cases pertaining to Configuration E, where the nucleation is obtained through the introduction of a shear stress asperity (see Appendix B for further details).

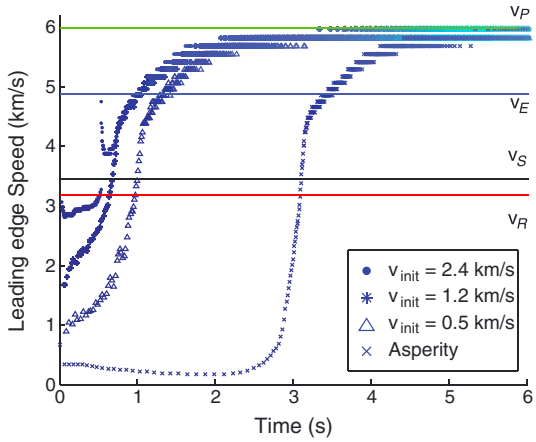

Figure B3. Comparison of rupture speeds using different rupture nucleation methods, for the case $S = 0.4$ and $\Delta x = 40$ m. Note that the only case in which the forbidden zone does exist (and the daughter front exhibits a jump) pertains to a case for which the initial rupture velocity is too high (2.4 km/s) and the nucleation procedure affects and pollutes the subsequent dynamic, spontaneous rupture propagation.

introduction of an initial shear stress asperity sections" of *Bizzarri* [2010], respectively, for a detailed discussion of these two strategies). The Configurations D and E (see Table 2) are relevant to this test.

For the Configuration D, the time-weakening method, a starting speed of $v_{init} = 1.2$ km/s is used, and the rupture speed curves are plotted in Figure B1. Compared to Configuration A (Figure 2), the nucleation stages have larger rupture speeds, but the spontaneous rupture behavior is similar. In particular, we do not observe any relevant change in the supershear transition.

For the Configuration E, an asperity nucleation method is used. The stress perturbation used to initialize the rupture is 0.5% greater than the upper yield stress. The asperity size is set to 2 L_C, where L_C is defined as the half-critical length in *Andrews* [1976] (see equation (1) of *Bizzarri* [2010]), and the entire asperity is allowed to rupture at the first time step to initiate the process. The resulting rupture speed curves are plotted in Figure B2, which shows that after the nucleation stage, the spontaneous rupture behavior is similar to Figures 2 and B1.

If v_{init} is large enough, the mother-daughter mechanism may act before direct supershear transition occurs, especially for small S ($S \leq \sim 0.72$). In such cases the penetration of forbidden zone disappears. An example of this situation is represented by a case with the time-weakening nucleation strategy, with a starting speed equal to 2.4 km/s and $\Delta x = 40$ m for the case of $S = 0.4$; the resulting rupture speed curve is plotted in Figure B3. Due to the larger starting speed the rupture speed jumps from sub-Rayleigh to supershear rupture speed via the mother-daughter mechanism. But for $S = 0.4$, all of the three ways of nucleation (time weakening with $v_{init} = 0.5$ km/s, 1.2 km/s, and asperity) show that the rupture speed increases continuously from sub-Rayleigh to supershear speed (Figure B3). This clearly indicates that if the initial rupture speed is too large (see also *Bizzarri* [2010]), the energy initially provided to the rupture is large enough to artificially cause an apparent jump of the daughter mechanism. This further confirms that the nucleation method, and the parameters controlling it, can have severe consequences in the subsequent rupture propagation. This is a clear example of a configuration in which the nucleation procedure artificially pollutes the solution and causes an improper rupture behavior. Incidentally, we also recall here that *Bizzarri* [2010] also found that if the initial shear asperity is too large (compared to the critical length of the problem), it might cause a supershear rupture speed also for large values of the strength parameter, which would theoretically predict a subshear rupture propagation. We emphasize that all the results presented and discussed in this paper (see section 3) pertain to a proper choice of the nucleation procedure, according to the general guidance of *Bizzarri* [2010].

Appendix C: Effect of Different Grid Sizes

In this section we will explore the effects of the adoption of different spatial discretization in the determination of the threshold value of the strength parameters S which separates the mother-daughter from the direct transition mechanisms.

When we change the spatial grid size Δx, but keep $C = v_P \Delta t / \Delta x$ unchanged, the time step Δt is automatically changed. To study the effect of different grid sizes, Configurations B and C are tested with $\Delta x = 20$ m and $\Delta x = 10$ m (see Table 2).

Compared to Configuration A (Figure 2), similar results are obtained in these two tests (Figure C1). The two regions that represent direct and mother-daughter supershear rupture transition are clearly seen. In the

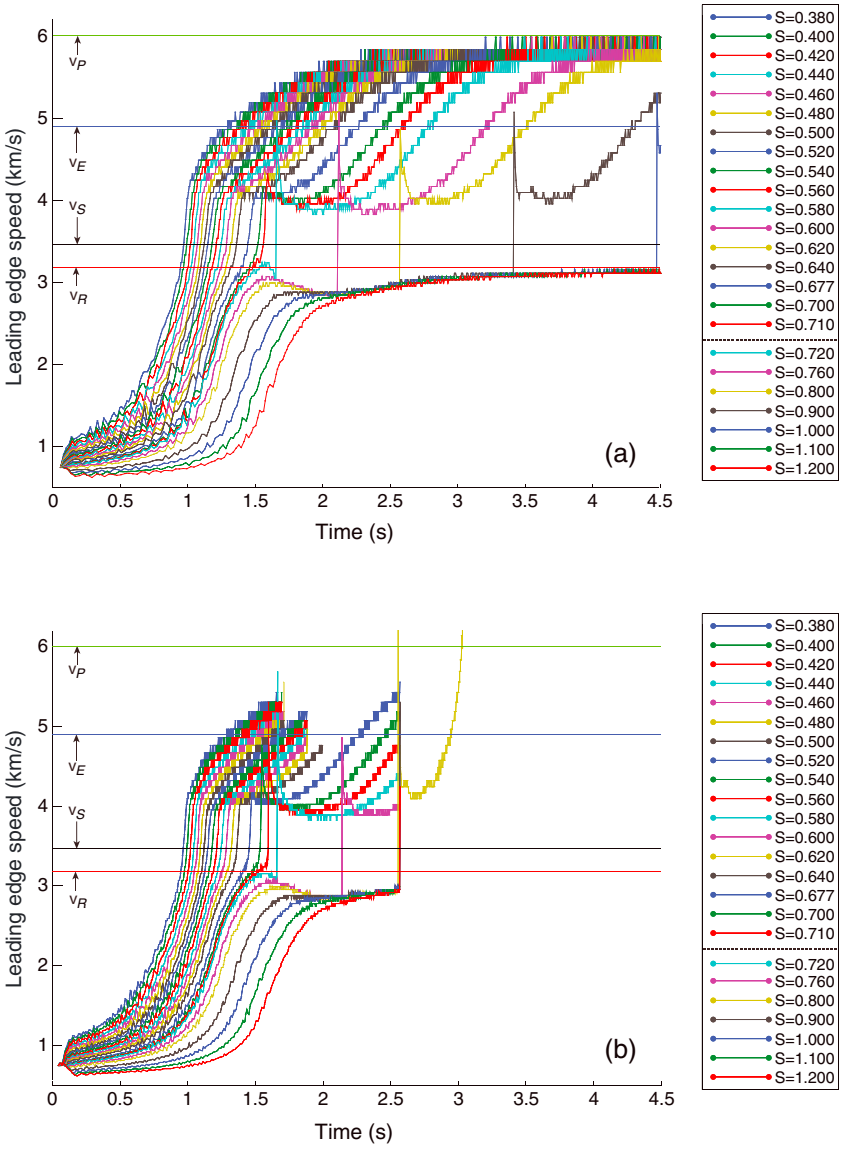

Figure C1. Rupture speeds for different spatial gird sizes in Configurations B and C, in which the rupture nucleation is obtained though the time-weakening method and the starting velocity is 0.5 km/s (see Appendix C for further details). (a) The Δx is 20 m. (b) The Δx is 10 m.

case of $S = 0.72$, the direct transition occurs in Configuration A, but the mother-daughter transition occurs in both Configurations B and C. This is due to the supershear transition being very sensitive to the stress peak. In the numerical simulations, the amplitude of the peak in stress field will increase as more high frequency components radiate from the rupture tip for smaller spatial grids. So the threshold value of S which separates the two different transition mechanisms changes from 0.76 to 0.72 as the spatial grid size decreases. This implies that in numerical simulations it is difficult to find an exact value of S (in an absolute sense) which separates the two parameter regions reported in Figure 2b. An estimation of about 0.7 is reasonable from our simulation results.

For smaller spatial grid size, the rupture speed curves are smoother—and this causes less numerical oscillations—but larger memory and more computational time are required in this case. In Configuration C, the simulation time is limited to 2.6 s, which is not long enough for the cases $S \geq 0.80$ to become supershear rupture. Balancing between computing time and accuracy, we choose spatial $\Delta x = 40$ m to simulate most of the cases.

Acknowledgments
C.L. is supported by the Newton International Fellowship 2012 of The Royal Society (NF120809). The authors would like to thank the Associate Editor and two anonymous reviewers for the many interesting comments and suggestions which improved and clarified the paper.

References

Aagaard, B. T., and T. H. Heaton (2004), Near-source ground motions from simulations of sustained intersonic and supersonic fault ruptures, *Bull. Seismol. Soc. Am.*, *94*, 2064–2078.
Abraham, F. F., and H. Gao (2000), How fast can cracks propagate?, *Phys. Rev. Lett.*, *84*, 3113–3116.
Andrews, D. J. (1973), A numerical study of tectonic stress release by underground explosions, *Bull. Seismol. Soc. Am.*, *63*(4), 1375–1391.
Andrews, D. J. (1976), Rupture velocity of plane strain shear cracks, *J. Geophys. Res.*, *81*(32), 5679–5687, doi:10.1029/JB081i032p05679.
Andrews, D. J. (1985), Dynamic plane-strain shear rupture with a slip-weakening friction law calculated by a boundary integral method, *Bull. Seismol. Soc. Am.*, *75*(1), 1–21.
Andrews, D. J. (1999), Test of two methods for faulting in finite-difference calculations, *Bull. Seismol. Soc. Am.*, *89*(4), 931–937.
Aochi, H., E. Fukuyama, and M. Matsu'ura (2000), Spontaneous rupture propagation on a non–planar fault in 3D elastic medium, *Pure Appl. Geophys.*, *157*, 2003–2027, doi:10.1007/PL00001072.
Archuleta, R. J. (1984), A faulting model for the 1979 Imperial Valley earthquake, *J. Geophys. Res.*, *89*(B6), 4559–4585, doi:10.1029/JB089iB06p04559.
Bhat, H. S., R. Dmowska, G. C. King, Y. Klinger, and J. R. Rice (2007), Off-fault damage patterns due to supershear ruptures with application to the 2001 M_w 8.1 Kokoxili (Kunlun) Tibet earthquake, *J. Geophys. Res.*, *112*, B06301, doi:10.1029/2006JB004425.
Bizzarri, A. (2010), How to promote earthquake ruptures: Different nucleation strategies in a dynamic model with slip-weakening friction, *Bull. Seismol. Soc. Am.*, *100*(3), 923–940, doi:10.1785/0120090179.
Bizzarri, A. (2011), On the deterministic description of earthquakes, *Rev. Geophys.*, *49*, RG3002, doi:10.1029/2011RG000356.
Bizzarri, A. (2013), Calculation of the local rupture speed of dynamically propagating earthquakes, *Ann. Geophys.*, *56*(5), S0560, doi:10.4401/ag-6279.
Bizzarri, A., and M. Cocco (2005), 3D dynamic simulations of spontaneous rupture propagation governed by different constitutive laws with rake rotation allowed, *Ann. Geophys.*, *48*(2), 279–299.
Bizzarri, A., and S. Das (2012), Mechanics of 3-D shear cracks between Rayleigh and shear wave rupture speeds, *Earth Planet. Sci. Lett.*, *357-358*, 397–404, doi:10.1016/j.epsl.2012.09.053.
Bizzarri, A., and P. Spudich (2008), Effects of supershear rupture speed on the high-frequency content of *S* waves investigated using spontaneous dynamic rupture models and isochrone theory, *J. Geophys. Res.*, *113*, B05304, doi:10.1029/2007JB005146.
Bizzarri, A., M. Cocco, D. Andrews, and E. Boschi (2001), Solving the dynamic rupture problem with different numerical approaches and constitutive laws, *Geophys. J. Int.*, *144*, 656–678, doi:10.1046/j.1365-246x.2001.01363.x.
Bizzarri, A., E. M. Dunham, and P. Spudich (2010), Coherence of Mach fronts during heterogeneous supershear earthquake rupture propagation: Simulations and comparison with observations, *J. Geophys. Res.*, *115*, B08301, doi:10.1029/2009JB006819.
Bouchon, M., and M. Vallée (2003), Observation of long supershear rupture during the magnitude 8.1 Kunlunshan earthquake, *Science*, *301*(5634), 824–826.
Bouchon, M., M. P. Bouin, H. Karabulut, M. N. Toksöz, M. Dietrich, and A. J. Rosakis (2001), How fast is rupture during an earthquake? New insights from the 1999 Turkey earthquakes, *Geophys. Res. Lett.*, *28*(14), 2723–2726, doi:10.1029/2001GL013112.
Broberg, K. B. (1994), Intersonic bilateral slip, *Geophys. J. Int.*, *119*, 706–714.
Broberg, K. B. (1995), Intersonic mode II crack expansion, *Arch. Mech.*, *47*, 859–871.
Broberg, K. B. (1999), *Cracks and Fracture*, Academic Press, London.
Burridge, R. (1973), Admissible speeds for plane-strain self-similar shear cracks with friction but lacking cohesion, *Geophys. J. Int.*, *35*(4), 439–455.
Burridge, R., G. Conn, and L. B. Freund (1979), The stability of a rapid mode II shear crack with finite cohesive traction, *J. Geophys. Res.*, *84*(B5), 2210–2222, doi:10.1029/JB084iB05p02210.
Das, S. (1976), A numerical study of rupture propagation and earthquake source mechanism, PhD thesis, Dep. of Earth and Planetary Sciences, Massachusetts Institute of Technology, Mass.
Das, S., and K. Aki (1977), A numerical study of two-dimensional spontaneous rupture propagation, *Geophys. J. Int.*, *50*(3), 643–668.
Dunham, E. M. (2007), Conditions governing the occurrence of supershear ruptures under slip-weakening friction, *J. Geophys. Res.*, *112*, B07302, doi:10.1029/2006JB004717.
Dunham, E. M., and R. J. Archuleta (2004), Evidence for a supershear transient during the 2002 Denali Fault earthquake, *Bull. Seismol. Soc. Am.*, *94*(6B), S256–S268.
Ellsworth, W., M. Celebi, J. Evans, E. Jensen, R. Kayen, M. Metz, D. Nyman, J. Roddick, P. Spudich, and C. Stephens (2004), Near-field ground motion of the 2002 Denali Fault, Alaska, earthquake recorded at Pump Station 10, *Earthquake Spectra*, *20*(3), 597–615.
Festa, G., and J. P. Vilotte (2006), Influence of the rupture initiation on the intersonic transition: Crack-like versus pulse-like modes, *Geophys. Res. Lett.*, *33*, L15320, doi:10.1029/2006GL026378.
Fliss, S., H. S. Bhat, R. Dmowska, and J. R. Rice (2005), Fault branching and rupture directivity, *J. Geophys. Res.*, *110*, B06312, doi:10.1029/2004JB003368.
Freund, L. B. (1979), The mechanics of dynamic shear crack propagation, *J. Geophys. Res.*, *84*(B5), 2199–2209, doi:10.1029/JB084iB05p02199.
Geubelle, P. H., and D. V. Kubair (2001), Intersonic crack propagation in homogeneous media under shear-dominated loading: Numerical analysis, *J. Mech. Phys. Solids*, *49*(3), 571–587.
Hamano, Y. (1974), Dependence of rupture-time history on heterogeneous distribution of stress and strength on fault plane (abstract), *Eos Trans. AGU*, *55*, 352.
Ida, Y. (1972), Cohesive force across the tip of a longitudinal-shear crack and Griffith's specific surface energy, *J. Geophys. Res.*, *77*(20), 3796–3805, doi:10.1029/JB077i020p03796.
Kame, N., J. R. Rice, and R. Dmowska (2003), Effects of prestress state and rupture velocity on dynamic fault branching, *J. Geophys. Res.*, *108*(B5), 2265, doi:10.1029/2002JB002189.
Liu, Y., and N. Lapusta (2008), Transition of mode II cracks from sub-Rayleigh to intersonic speeds in the presence of favorable heterogeneity, *J. Mech. Phys. Solids*, *56*(1), 25–50.
Lu, X., N. Lapusta, and A. J. Rosakis (2007), Pulse-like and crack-like ruptures in experiments mimicking crustal earthquakes, *Proc. Natl. Acad. Sci. U.S.A.*, *104*(48), 18,931–18,936.
Lu, X., N. Lapusta, and A. J. Rosakis (2009), Analysis of supershear transition regimes in rupture experiments: The effect of nucleation conditions and friction parameters, *Geophys. J. Int.*, *177*(2), 717–732.
Mitchell, A. R. (1976), *Computational Methods in Partial Differential Equations*, Wiley, New York.
Olsen, K. B., R. Madariaga, and R. J. Archuleta (1997), Three-dimensional dynamic simulation of the 1992 Landers earthquake, *Science*, *278*(5339), 834–838.

Passelègue, F. X., A. Schubnel, S. Nielsen, H. S. Bhat, and R. Madariaga (2013), From sub-Rayleigh to supershear ruptures during stick-slip experiments on crustal rocks, *Science*, *340*(6137), 1208–1211.

Poliakov, A. N. B., R. Dmowska, and J. R. Rice (2002), Dynamic shear rupture interactions with fault bends and off-axis secondary faulting, *J. Geophys. Res.*, *107*(B11), 2295, doi:10.1029/2001JB000572.

Robinson, D. P., C. Brough, and S. Das (2006), The Mw 7.8, 2001 Kunlunshan earthquake: Extreme rupture speed variability and effect of fault geometry, *J. Geophys. Res.*, *111*, B08303, doi:10.1029/2005JB004137.

Robinson, D. P., S. Das, and M. P. Searle (2010), Earthquake fault superhighways, *Tectonophysics*, *493*(3), 236–243.

Rosakis, A. J. (2002), Intersonic shear cracks and fault ruptures, *Adv. Phys.*, *51*(4), 1189–1257.

Rosakis, A. J., O. Samudrala, and D. Coker (1999), Cracks faster than the shear wave speed, *Science*, *284*(5418), 1337–1340.

Rosakis, A., K. Xia, G. Lykotrafitis, and H. Kanamori (2007), Dynamic shear rupture in frictional interfaces: Speeds, directionality and modes, *Treatise Geophys.*, *4*, 153–192.

Vallée, M., M. Landès, N. M. Shapiro, and Y. Klinger (2008), The 14 November 2001 Kokoxili (Tibet) earthquake: High-frequency seismic radiation originating from the transitions between sub-Rayleigh and supershear rupture velocity regimes, *J. Geophys. Res.*, *113*, B07305, doi:10.1029/2007JB005520.

Xia, K., A. J. Rosakis, and H. Kanamori (2004), Laboratory earthquakes: The sub-Rayleigh-to-supershear rupture transition, *Science*, *303*(5665), 1859–1861.

Xia, K., A. J. Rosakis, H. Kanamori, and J. R. Rice (2005), Laboratory earthquakes along inhomogeneous faults: Directionality and supershear, *Science*, *308*, 681–684.